nanomaterials

MDPI

Article

Strain-Tunable Visible-Light-Responsive Photocatalytic Properties of Two-Dimensional CdS/g-C_3N_4: A Hybrid Density Functional Study

Guangzhao Wang [1,*], Feng Zhou [1], Binfang Yuan [2,*], Shuyuan Xiao [3], Anlong Kuang [4,*], Mingmin Zhong [4], Suihu Dang [1], Xiaojiang Long [1] and Wanli Zhang [1]

1 School of Electronic Information Engineering, Key Laboratory of Extraordinary Bond Engineering and Advanced Materials Technology of Chongqing, Yangtze Normal University, Chongqing 408100, China; zhoufeng9966@126.com (F.Z.); dangsuihu@126.com (S.D.); longxiaojiang@yznu.edu.cn (X.L.); zhangwl@yznu.cn (W.Z.)
2 School of Chemistry and Chemical Engineering, Yangtze Normal University, Chongqing 408100, China
3 Institute for Advanced Study, Nanchang University, Nanchang 330031, China; syxiao@hust.edu.cn
4 School of Physical Science and Technology, Southwest University, Chongqing 400715, China; zhongmm@swu.edu.cn
* Correspondence: wangyan6930@yznu.edu.cn or wangyan6930@126.com (G.W.); 6781022@163.com (B.Y.); alkuang@swu.edu.cn (A.K.)

Received: 9 January 2019; Accepted: 5 February 2019; Published: 12 February 2019

Abstract: By means of a hybrid density functional, we comprehensively investigate the energetic, electronic, optical properties, and band edge alignments of two-dimensional (2D) CdS/g-C_3N_4 heterostructures by considering the effect of biaxial strain and pH value, so as to improve the photocatalytic activity. The results reveal that a CdS monolayer weakly contacts with g-C_3N_4, forming a type II van der Waals (vdW) heterostructure. The narrow bandgap makes CdS/g-C_3N_4 suitable for absorbing visible light and the induced built-in electric field between the interface promotes the effective separation of photogenerated carriers. Through applying the biaxial strain, the interface adhesion energy, bandgap, and band edge positions, in contrast with water, redox levels of CdS/g-C_3N_4 can be obviously adjusted. Especially, the pH of electrolyte also significantly influences the photocatalytic performance of CdS/g-C_3N_4. When pH is smaller than 6.5, the band edge alignments of CdS/g-C_3N_4 are thermodynamically beneficial for oxygen and hydrogen generation. Our findings offer a theoretical basis to develop g-C_3N_4-based water-splitting photocatalysts.

Keywords: CdS/g-C_3N_4; strain-tunable; photocatalysis; water splitting; hybrid density functional

1. Introduction

Gaining hydrogen through photocatalytic water splitting by use of solar energy provides a new way to solve the problems of energy shortage and environmental pollution. A large number of semiconductors, such as TiO_2 [1], ZnO [2], $KNbO_3$ [3], and $NaNbO_3$ [4] have drawn much attention as promising photocatalysts, but they can merely utilize ultraviolet light, which only makes up only 4% of solar energy. Some photocatalysts, such as bulk CdS [5], have suitable bandgaps for visible light absorption, but lacks stability due to the self-oxidation of photogenerated species. Thus, it is challenging to find efficient water-splitting photocatalysts, and some appropriate strategies should be taken to modulate the electronic and photocatalytic properties of pristine photocatalysts. Generally, introduction of dopants [6,7], loading noble metal [8], dye sensitizing [9] and cocatalysis through constructing heterojunctions [10–12] are effective at improving the photocatalytic activity. The desired photocatalyst must have the conduction band minimum (CBM) and valence band maximum (VBM)

individually above the water reduction (H^+/H_2) potential and below the water oxidation (O_2/H_2O) potential. Besides, the theoretical minimum bandgap of 1.23 eV is required for water splitting [13] considering the overpotential accompanied by water redox processes.

Since graphene was prepared, 2D materials including hexagonal boron nitride [14], graphite-like zinc oxide [15], transition-metal dichalcogenides [16], and MXenes [17] have been extensively investigated and utilized in the area of optoelectronics and photocatalysts. Particularly, the graphite-like carbon nitride (g-C_3N_4) is a prospective photocatalyst used for hydrogen generation by photocatalytic decomposition of water [18]. g-C_3N_4 has a suitable bandgap of 2.7 eV for visible light absorption. However, g-C_3N_4 exhibits poor photocatalytic efficiency because of the fast recombination of photogenerated electron–hole pairs [19–21]. This factor obviously restrains the photocatalytic efficiency of g-C_3N_4. It is of great significance to adopt measures to regulate the electronic structures of g-C_3N_4 in a bid to enhance the photocatalytic performance. Especially, a large number of 2D heterostructures, such as ZnO/WS_2 [22], AlN/WS_2 [23], GaN/WS_2 [24], g-C_6N_6/g-C_3N_4 [25], g-C_3N_4/MoS_2 [26] and g-C_3N_4/C_2N [27] exhibit significantly improved photocatalytic activity as compared to pristine 2D materials. In these heterostructures, the formed built-in electric field caused by the charge accumulation/depletion around the interfaces promotes the effective separation and migration of photogenerated carriers, which is beneficial to enhance the photocatalytic performance. A recent theoretical study [28] reports the stability, electronic structures, and offset of 2D CdS/g-C_3N_4 heterostructure, and the result suggests that the heterostructure has suitable bandgap and band alignments for visible light photocatalytic water splitting. Moreover, the induced electric field between CdS layer and g-C_3N_4 also accelerates the separation of photogenerated carriers and improves the photocatalytic activity. However, whether the biaxial strain will improve the photocatalytic activity of CdS/g-C_3N_4 is still unclear. Besides, it is also unclear whether the photocatalytic activity of CdS/g-C_3N_4 is affected by the pH of electrolyte. These two problems have to be solved in a bid to obviously enhance the photocatalytic performance of CdS/g-C_3N_4.

The purpose of this work is to investigate the energetic, electronic, optical property and band edge alignments of CdS/g-C_3N_4 as well as the effect induced by the biaxial strain and the pH of electrolyte, in order to regulate the photocatalytic performance. This work is organized as follows. Section 2 depicts the computational details, while Section 3 displays the results and discussion about the energetic, optical, optical, band edge alignments as well as the photocatalytic property of CdS/g-C_3N_4 heterostructure with the consideration of biaxial strain and pH, and ultimately Section 4 lists some concluding remarks.

2. Computational Details

The CdS/g-C_3N_4 heterostructure, which consists of 3 Cd, 3 S, 6 C, and 8 N atoms, is constructed through vertically stacking a $\sqrt{3} \times \sqrt{3}$ supercell of hexagonal CdS single-layer on a 1×1 g-C_3N_4 cell. We carry out density functional theory (DFT) calculations by means of the general gradient approximation (GGA) [29] of Perdew–Burke–Ernzerhof (PBE) [30] and hybrid density functional of HSE06 [31], as implemented in the Vienna ab initio simulation package (VASP) [32]. We adopt the projected-augmented-wave (PAW) method [33] to describe the electron-ion interaction and DFT-D3 correction [34] to well treat long-range vdW interaction. To avoid the interactions introduced by the periodic structures, a vacuum of 18 Å is used. We first optimize the geometries by use of PBE, and then accurately calculate the electronic and optical properties by utilization of HSE06. The plane-wave cutoff energy is set as 500 eV, and a Monkhorst-pack [35] k-point mesh of $13 \times 13 \times 1$ for CdS cell, $9 \times 9 \times 1$ for g-C_3N_4 cell and CdS/g-C_3N_4 heterostructures are used. All the structures are fully relaxed until the energy and force on each atom are individually reduced to 10^{-5} eV and 0.02 eV/Å. The valence electron configurations of of Cd ($4d^{10}5s^2$), S ($3s^23p^4$), C($2s^22p^2$), and N ($2s^22p^3$) are considered to construct the PAW potentials.

Finally, the optical absorption spectra of g-C_3N_4 and CdS/g-C_3N_4 composite is calculated by use of HSE06. The absorption coefficient is obtained from the the real and imaginary parts of the frequency dependent complex dielectric function $\varepsilon(\omega)=\varepsilon_1(\omega)+i\varepsilon_2(\omega)$ according to the following relationship [36]

$$I(\omega) = \sqrt{2}\omega\sqrt{\sqrt{\varepsilon_1^2(\omega)+\varepsilon_2^2(\omega)}-\varepsilon_1(\omega)} \quad (1)$$

The imaginary part of the dielectric function ε_2 is calculated as [37]

$$\varepsilon_2(\hbar\omega) = \frac{2e^2\pi}{\Omega\varepsilon_0}\sum_{k,v,c}|\langle\psi_k^c|\mathbf{u}\cdot\mathbf{r}|\psi_k^v\rangle|^2\delta(E_k^c-E_k^v-\hbar\omega) \quad (2)$$

where Ω, v, c, ω, $\mathbf{u}$, ψ_k^v and ψ_k^c denotes the unit-cell volume, valence bands, conduction bands, photon frequencies, the vector defining the polarization of the incident electric field, the occupied and unoccupied wave functions at point k in reciprocal space, respectively, while the real part of the dielectric function ε_1 can be obtained from imaginary part ε_2 by the Kramer-Kronig relationship [38].

$$\varepsilon_1(\omega) = 1+\frac{2}{\pi}p\int_0^\infty\frac{\varepsilon_2(\omega')\omega'}{\omega'^2-\omega^2}d\omega' \quad (3)$$

where p denotes the principal value of the integral.

3. Results and Discussion

The geometry structures, density of states (DOS) and projected density of states (PDOS) of CdS monolayer and g-C_3N_4 are depicted in Figure 1. The calculated lattice constants for CdS and g-C_3N_4 single-layers are respectively a = b = 4.245 and a = b = 7.134 Å, and the obtained bandgaps for CdS and g-C_3N_4 single-layers are, respectively, 2.74 and 2.77 eV, which are well consistent with previous experiment and theoretical reports [28]. The VBM of CdS single-layer mainly consists of S 3p, Cd 4d and Cd 4p orbitals, whereas the CBM is primarily contributed by Cd 5s character. For g-C_3N_4, the VBM is mainly composed of N 2p orbitals with some amount of C 2p and N 2s orbitals, while the CBM is comprised of C 2p and N 2p characters.

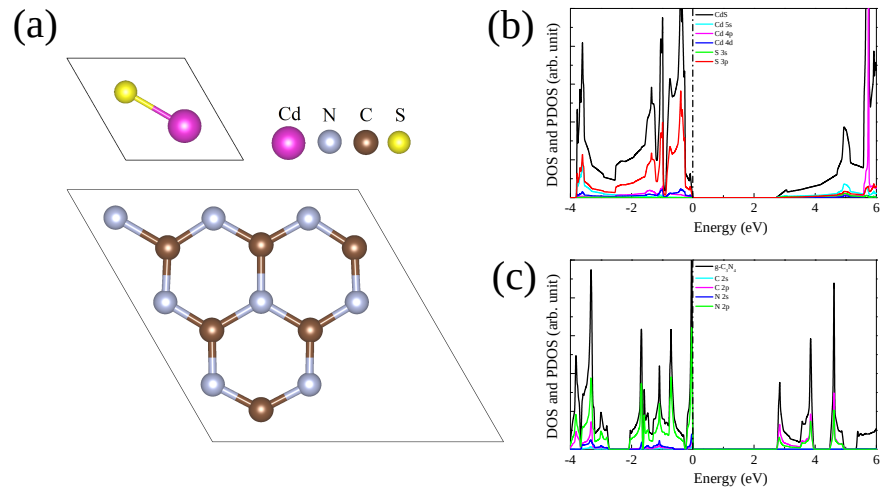

Figure 1. (**a**) Crystal structures of CdS single-layer and g-C_3N_4. DOS and PDOS of (**b**) CdS single-layer and (**c**) g-C_3N_4.

The lattice mismatch is defined as: $[(L_{g-C_3N_4}-L_{s-CdS})/L_{s-CdS}]\times 100\%$, where $L_{g-C_3N_4}$ and L_{s-CdS} are the lattice constants of g-C_3N_4 cell and $\sqrt{3}\times\sqrt{3}$ CdS supercell, respectively. When a $\sqrt{3}\times\sqrt{3}$ CdS supercell contacts with a 1×1 g-C_3N_4 cell, the lattice mismatch is only -2.97%, which is

good for the construction of CdS/g-C_3N_4 heterostructure. We consider a $\sqrt{3} \times \sqrt{3}$ CdS supercell with with tree special rotation angles of 0°, 120°, and 240° sitting on a 1×11 g-C_3N_4 cell with fixed angles to construct three possible configurations of CdS/g-C_3N_4, as depicted in Figure 2. These different heterostructures are call as CdS/g-C_3N_4 (i), (ii), and (iii), respectively. The optimized lattice constants for CdS/g-C_3N_4 (i), (ii) and (iii) are respectively 6.954, 6.955 and 6.920 Å, slightly smaller than the lattice of g-C_3N_4. This may be attributed to the atom rearrangements in the heterostructures. The obtained bandgaps for CdS/g-C_3N_4 (i), (ii) and (iii) are 2.745, 2.746 and 2.676 eV, respectively. Though the bandgaps of these heterostructures are almost the same as the bandgap of g-C_3N_4, the absorption of visible light is significantly improved. This will be detailed in the following discussion.

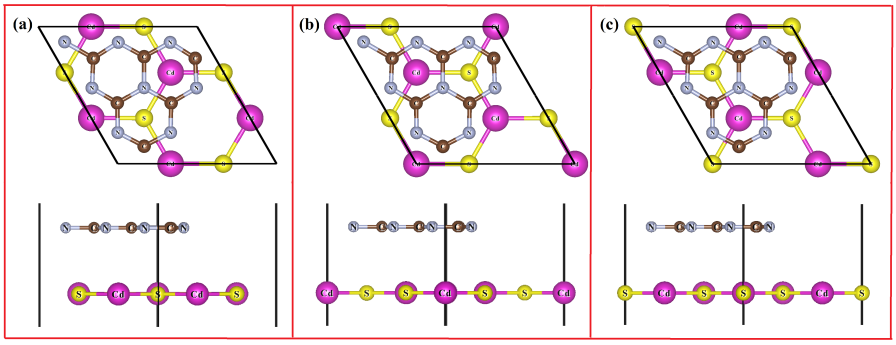

Figure 2. Top and side views of three possible stackings of CdS/g-C_3N_4 heterostructures.

To explore the thermodynamic stability, the interface binding energy (E_b) is calculated according to the following relationship:

$$E_b = E_{\text{CdS/g-}C_3N_4} - E_{\text{CdS}} - E_{\text{g-}C_3N_4} \tag{4}$$

where $E_{\text{CdS/g-}C_3N_4}$, E_{CdS}, and $E_{\text{g-}C_3N_4}$ denote the total energies of CdS/g-C_3N_4 heterostructure, CdS single-layer, and g-C_3N_4, respectively. The E_b values for CdS/g-C_3N_4 (i), (ii) and (iii) are respectively −1.62633, −1.62548 and −1.62630 eV, implying these heterostructures are exothermic and are energetically favorable. Besides, the differences of E_b among these structures are so small that these three configurations may be experimentally prepared at the same time. These three configurations have similar energy values. Furthermore, the band alignments depicted in Figure 3 also indicate that the band edge positions of these three heterostructures are close. Thus, our discussion is mainly focused on the CdS/g-C_3N_4 (i). The interface adhesion energy (E_a) is calculated according to the following equation:

$$E_a = E_b / S \tag{5}$$

where S is the area of CdS/g-C_3N_4 heterostructure vertical to the vacuum direction. The E_a for CdS/g-C_3N_4 (i) is −19.4 meV/Å^2, within the scope of typical vdW heterostructure of −20 meV/Å^2 [39].

As an ideal water-splitting photocatalyst, its band edges must be located in proper positions. The CBM and VBM must straddle the water redox potentials to satisfy the thermodynamic criterion for overall water splitting. Figure 3 displays the band edge alignments for CdS monolayer, g-C_3N_4, CdS/g-C_3N_4 (i), (ii) and (iii). The band edges of these systems are all straddle the water redox levels, which is propitious to spontaneously produce both hydrogen and oxygen.

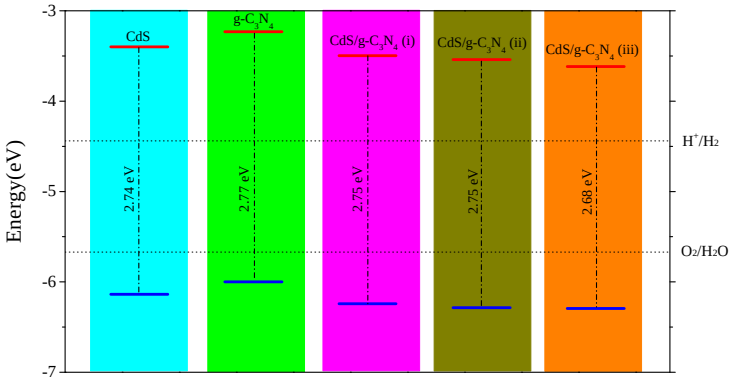

Figure 3. Band edge alignments for CdS single-layer, g-C_3N_4, CdS/g-C_3N_4 (i), (ii), and (iii) in contrast with water redox levels.

The appearance of strain can not be ignored due to the lattice mismatch between different 2D semiconductors. It is found that for 2D materials, the electronic and optical properties can be modulated through strain engineering [40–42]. We consider the influence caused by both tensile and compressive biaxial strain on the energetic, electronic, and photocatalytic properties of CdS/g-C_3N_4. The biaxial strain is defined as $\epsilon = [(a - a_0)/a_0] \times 100\%$, in which a and a_0 are the lattice parameters of strained and pristine CdS/g-C_3N_4 heterostructures, respectively. $\epsilon < 0$ means the structure is compressed, while $\epsilon > 0$ means the structure is stretched. Figure 4 gives the varied E_a and E_g values of CdS/g-C_3N_4 heterostructures of different biaxial strain with 2% apart. The E_a value gets smaller within the scope of $\epsilon = -8\%$ to $\epsilon = 0$ but gets larger in the range of $\epsilon = 0$ to $\epsilon = 8\%$. The unstrained CdS/g-C_3N_4 heterostructure has the least interface adhesion energy, which implies that unstrained configuration has advantage in energy in contrast with strained configuration. The calculated E_a value with the ϵ in the range from -8% to 8% are 82.2, 55.1, 7.1, -11.8, -19.4, -11.7, 6.8, 32.9 and 52.8 meV/Å^2, indicating the formation of the heterostructures with the $\epsilon = -2\%$, 0, 2% are exothermic. The E_g value decreases in the range of $\epsilon = -8\%$ to $\epsilon = -6\%$, increases in the range of $\epsilon = -6\%$ to $\epsilon = 0$, and decreases in the range of $\epsilon = 0$ to $\epsilon = 8\%$. This suggests that the visible light absorption can be modulated by tuning the bandgaps through biaxial strain engineering. The unstrained heterostructure has the largest bandgap. The obtained bandgaps for CdS/g-C_3N_4 heterostructures in the range of $\epsilon = -8\%$ to $\epsilon = 8\%$ are 2.43, 0.78, 1.72, 2.19, 2.75, 2.54, 2.34, 2.20 and 1.34 eV.

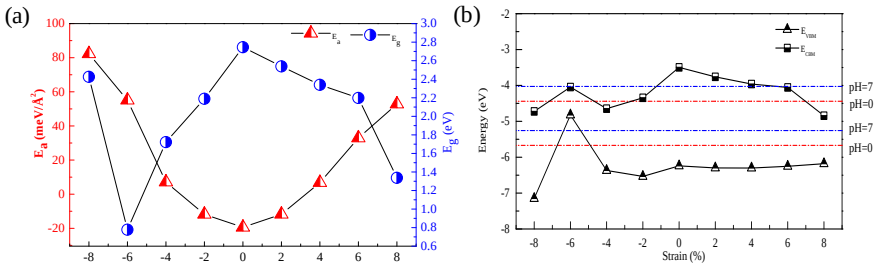

Figure 4. (**a**) Varied interface adhesion energies (E_a) and bandgaps (E_g) of CdS/g-C_3N_4 heterostructures with different biaxial strains. (**b**) Band edge alignments of CdS/g-C_3N_4 heterostructures with different biaxial strains. The red and blue horizontal lines are the water redox potentials as pH = 0 and pH = 7, respectively.

The photocatalytic performance is affected by the pH of electrolyte. Particularly, the standard hydrogen electrode potential varies with the pH varies. The standard reduction (H^+/H_2) in contrast with the vacuum level is calculated by: $E_{H^+/H_2} = -4.44$ eV + pH $\times$ 0.059 eV [43]. With the consideration of the difference of 1.23 eV [44] between water redox potentials during the water redox reactions, the oxygen potential (O_2/H_2O) is calculated by: $E_{O_2/H_2O} = E_{H^+/H_2} - 1.23$ eV =

-5.67 eV + pH $\times$ 0.059 eV. The method has been successfully applied to predict the photocatalytic properties of P and As doped C_2N monolayer [45], CdS/ZnSe heterostructure [46], and (Bule P)/BSe heterostructure [47] with considering the effect of pH on the standard redox potentials with respect to the vacuum level.

The band edge alignments of CdS/g-C_3N_4 heterostructures with diverse biaxial strains are displayed in Figure 4. Both CBM and VBM of CdS/g-C_3N_4 of $\epsilon = -2\%$, 0, 2%, 4%, 6% individually straddle the water redox levels in the pH range of 0–1.6, 0–14, 0–11.5, 0–8.1, 0–6.5. In the pH range of 0–14, the VBM and CBM of CdS/g-C_3N_4 with $\epsilon = -8\%$, -4%, 8% are individually lower than the water oxidation (O_2/H_2O) and reduction (H^+/H_2) potentials, which means that these heterostructures are only beneficial for oxygen generation. For the case of $\epsilon = -6\%$, the VBM and CBM are individually above the water oxidation (O_2/H_2O) and reduction (H^+/H_2) potentials when the pH is lower than 6.9. When the pH is lower than 6.5, the CdS/g-C_3N_4 with ϵ = 0, 2%, 4%, 6% are thermodynamically feasible for over all water redox reactions, while the composites of $\epsilon = -2\%$, -6%, -8%, -4%, 8% are propitious to spontaneously generate oxygen. Therefore, adjustment of the pH lower than 6.5 is conducive to improve the photocatalytic activity of CdS/g-C_3N_4.

Next, we plot the DOS, PDOS, and band structures of unstrained CdS/g-C_3N_4 to shed light on the physical mechanism of water splitting of CdS/g-C_3N_4. Figure 5 shows that the CBM and VBM are individually donated by g-C_3N_4 and CdS layer, suggesting that the CdS/g-C_3N_4 is a type II heterostructure. The partial charge density of CBM and VBM in Figure 6 also suggests the CBM of g-C_3N_4 is predominately contributed by g-C_3N_4 and the VBM is mainly donated by CdS layer. The VBM is primarily composed of S 3p, Cd 4d and Cd 4p states, while the CBM is predominately dominated by N 2p and C 2p states. Taking the electronic transition of angular momentum selection rules of $\triangle l = \pm 1$ into account, after absorbing photons, the electrons primarily migrate from Cd 4d orbitals below the Fermi level to N 2p and C 2p orbitals in conduction band.

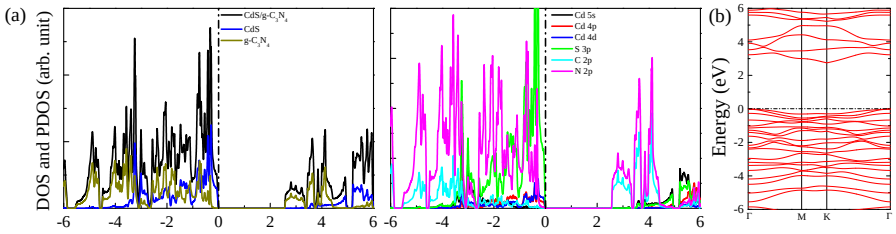

Figure 5. (**a**) DOS, PDOS and (**b**) band structures of CdS/g-C_3N_4 heterostructure.

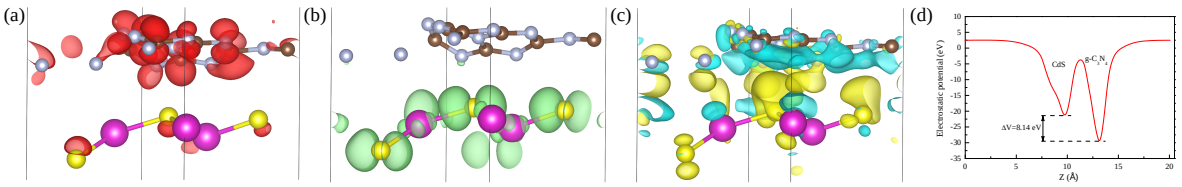

Figure 6. Partial charge densities of (**a**) CBM, (**b**) VBM, (**c**) the charge density difference, and (**d**) potential drop across the interface of CdS/g-C_3N_4 heterostructure.

The charge density difference of CdS/g-C_3N_4 heterostructure in Figure 6c, where cyan and yellow regions represent charge depletion and accumulation, respectively. It is obvious that electrons migrate from CdS layer to g-C_3N_4. Based on the Bader charge analysis, the transferred charge is 0.027 $|e|$, which is enough to introduce a large potential drop between the g-C_3N_4 and CdS layer. Figure 6d lists potential drop across the interface of CdS/g-C_3N_4 along the Z direction, i.e., the vacuum direction. The g-C_3N_4 has a deeper potential as compared to that of CdS layer, which drives electrons to migrate from CdS layer to g-C_3N_4. The potential drop (ΔV) across the interface is 8.14 eV, inducing a built-in electric field from the g-C_3N_4 to CdS layer. The formed built-in electric field can promote the shifts

of photogenerated carriers, thus further inhibiting the recombination of photogenerated carriers. The g-C_3N_4 and CdS individually pose as electron acceptor and donor. Thus, the water oxidation reaction and reduction reaction occur on the CdS layer and g-C_3N_4, respectively. This is beneficial for improving the photocatalytic activity.

Another key indicator to the photocatalytic performance is the optical absorption. Figure 7 depicts the obtained absorption cures for g-C_3N_4 and CdS/g-C_3N_4, the original g-C_3N_4 only exhibits a obvious absorption above 3.0 eV and there is almost no visible light absorption ability for g-C_3N_4, which may be due to the fact that only a small amount of electron density migrates electron migrates from N 2s states of valence band to C 2p and N 2p states of conduction band (see Figure 1). The adsorption edge of CdS/g-C_3N_4 shifts to 2.7 eV, especially the g-C_3N_4 shows stronger light absorption than g-C_3N_4 in the range of 2.7–4.3 eV, i.e., the CdS/g-C_3N_4 owns a broad absorption in both ultraviolet and visible light regions. According to Figures 1 and 5, the reason of enhancement of light absorption should be that the electron migration from the Cd 4d states below the Fermi level to C 2p and N 2p states are significantly enhanced as compared to pristine g-C_3N_4.

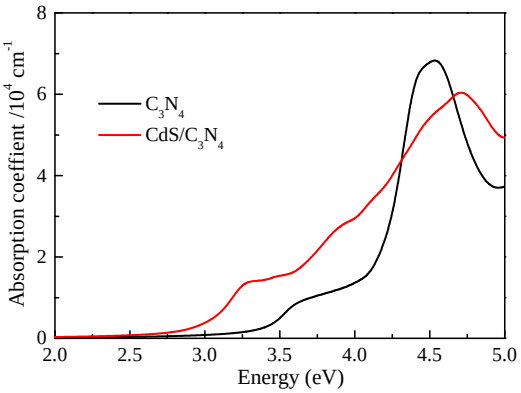

Figure 7. Absorption spectra of pristine g-C_3N_4 and CdS/g-C_3N_4 heterostructure.

4. Conclusions

In summary, the hybrid density functional HSE06 is employed to calculate the energetic, electronic and optical properties of CdS/g-C_3N_4, whilst taking into account different biaxial strains as well as the pH of electrolyte, in a bid to tune the photocatalytic activity of CdS/g-C_3N_4. When the interaction between single-layer CdS and g-C_3N_4, the vdW CdS/g-C_3N_4 heterostructure is easy to form, as the interface adhesion formation energy is negative. The predicted bandgaps and optical absorptions indicate the CdS/g-C_3N_4 heterostructure can absorb visible light. Furthermore, the formed built-in electric field around the interface region is helpful to accelerate electron–hole recombination. The bandgaps, interface adhesion energies, and band edge alignments in reference to water redox potentials are visibly affected by the biaxial strains. The photocatalytic performance of CdS/g-C_3N_4 can be modulated by tuning the biaxial strains and pH. When pH is lower than 6.5, the band edge positions of CdS/g-C_3N_4 are thermodynamically favorable for spontaneously producing of oxygen and hydrogen. In general, CdS/g-C_3N_4 is a perspective water-splitting photocatalyst.

Author Contributions: G.W., B.Y., and A.K. designed the project, guided the study, and prepared the manuscript; F.Z., S.X., and M.Z. carried the calculations; S.D., X.L. and W.Z. analyzed the calculated results and produced the illustrations.

Funding: This work was supported by the National Natural Science Foundation of China under Grant Nos. 11504301 and 11847100, and the Science and Technology Plan Project of Fuling District under Grant No. FLKJ,2018BBA3056.

Acknowledgments: The work was carried out at LvLiang Cloud Computing Center of China, and the calculations were performed on TianHe-2.

Conflicts of Interest: The authors declare no conflict of interest.

References

1. Yin, W.; Wei, S.; Aljassim, M.M.; Yan, Y. Double-hole-mediated coupling of dopants and its impact on band gap engineering in TiO_2. *Phys. Rev. Lett.* **2011**, *106*, 066801. [CrossRef] [PubMed]
2. Pan, J.; Wang, S.; Chen, Q.; Hu, J.; Wang, J. Band-structure engineering of ZnO by anion-cation co-doping for enhanced photo-electrochemical activity. *ChemPhysChem* **2014**, *15*, 1611–1618. [CrossRef] [PubMed]
3. Wang, G.; Chen, H.; Li, Y.; Kuang, A.; Yuan, H.; Wu, G. A hybrid density functional study on the visible light photocatalytic activity of (Mo,Cr)-N codoped $KNbO_3$. *Phys. Chem. Chem. Phys.* **2015**, *17*, 28743–28753. [PubMed]
4. Wang, G.; Chen, H.; Wu, G.; Kuang, A.; Yuan, H. Hybrid density functional study on mono- and codoped $NaNbO_3$ for visible-light photocatalysis. *ChemPhysChem* **2016**, *17*, 489–499. [CrossRef] [PubMed]
5. Liu, J. Origin of high photocatalytic efficiency in monolayer g-C_3N_4/CdS heterostructure: a hybrid DFT study. *J. Phys. Chem. C* **2015**, *119*, 28417–28423. [CrossRef]
6. Wang, G.; Huang, Y.; Kuang, A.; Yuan, H.; Li, Y.; Chen, H. Double-hole-mediated codoping on $KNbO_3$ for visible light photocatalysis. *Inorg. Chem.* **2016**, *55*, 9620–9631. [CrossRef] [PubMed]
7. Gai, Y.; Li, J.; Li, S.; Xia, J.; Wei, S. Design of narrow-gap TiO_2: A passivated codoping approach for enhanced Pphotoelectrochemical activity. *Phys. Rev. Lett.* **2009**, *102*, 036402. [CrossRef]
8. Meir, N.; Plante, I.J.; Flomin, K.; Chockler, E.; Moshofsky, B.; Diab, M.; Volokh, M.; Mokari, T. Studying the chemical, optical and catalytic properties of noble metal (Pt, Pd, Ag, Au)-Cu_2O core-shell nanostructures grown via a general approach. *J. Mater. Chem.* **2013**, *1*, 1763–1769. [CrossRef]
9. Leijtens, T.; Lim, J.; Teuscher, J.; Park, T.; Snaith, H.J. Charge density dependent mobility of organic hole-transporters and mesoporous TiO_2 determined by transient mobility spectroscopy: implications to dye-sensitized and organic solar cells. *Adv. Mater.* **2013**, *25*, 3227–3233. [CrossRef]
10. Yang, W.; Wen, Y.; Zeng, D.; Wang, Q.; Chen, R.; Wang, W.; Shan, B. Interfacial charge transfer and enhanced photocatalytic performance for the heterojunction WO_3/BiOCl: First-principles study. *J. Mater. Chem.* **2014**, *2*, 20770–20775. [CrossRef]
11. Torabi, A.; Staroverov, V.N. Band gap reduction in ZnO and ZnS by creating layered ZnO/ZnS heterostructures. *J. Phys. Chem. Lett.* **2015**, *6*, 2075–2080. [CrossRef] [PubMed]
12. Cui, X.; Yang, X.; Xian, X.; Tian, L.; Tang, H.; Liu, Q. Insights into highly improved solar-driven photocatalytic oxygen evolution over integrated Ag_3PO_4/MoS_2 heterostructures. *Front. Chem.* **2018**, *6*, 123. [CrossRef] [PubMed]
13. Liao, J.; Sa, B.; Zhou, J.; Ahuja, R.; Sun, Z. Design of high-efficiency visible-light photocatalysts for water splitting: MoS_2/AlN(GaN) heterostructures. *J. Phys. Chem. C* **2014**, *118*, 17594–17599. [CrossRef]
14. Golberg, D.; Bando, Y.; Huang, Y.; Terao, T.; Mitome, M.; Tang, C.; Zhi, C. Boron nitride nanotubes and nanosheets. *ACS Nano* **2010**, *4*, 2979–2993. [CrossRef] [PubMed]
15. Wang, G.; Yuan, H.; Chang, J.; Wang, B.; Kuang, A.; Chen, H. ZnO/MoX_2 (X = S, Se) composites used for visible light photocatalysis. *RSC Adv.* **2018**, *8*, 10828–10835. [CrossRef]
16. Chhowalla, M.; Shin, H.S.; Eda, G.; Li, L.; Loh, K.P.; Zhang, H. The chemistry of two-dimensional layered transition metal dichalcogenide nanosheets. *Nat. Chem.* **2013**, *5*, 263–275. [CrossRef] [PubMed]
17. He, J.; Ding, G.; Zhong, C.; Li, S.; Li, D.; Zhang, G. Cr_2TiC_2-based double MXenes: Novel 2D bipolar antiferromagnetic semiconductor with gate-controllable spin orientation toward antiferromagnetic spintronics. *Nanoscale* **2019**, *11*, 356–364. [CrossRef]
18. Wang, X.; Maeda, K.; Thomas, A.; Takanabe, K.; Xin, G.; Carlsson, J.M.; Domen, K.; Antonietti, M. A metal-free polymeric photocatalyst for hydrogen production from water under visible light. *Nat. Chem.* **2009**, *8*, 76–80. [CrossRef]
19. Zhang, M.; Yao, W.; Lv, Y.; Bai, X.; Zhu, Y. Enhancement of mineralization ability of C_3N_4 via a lower valence position by a tetracyanoquinodimethane organic semiconductor. *J. Mater. Chem. A* **2014**, *2*, 11432–11438. [CrossRef]
20. Liang, Y.; Long, C.; Li, J.; Huang, B.; Dai, Y. InSe monolayer: Promising cocatalyst of g-C_3N_4 for water splitting under Visible Light. *ACS Appl. Energy Mater.* **2018**, *1*, 5394–5401. [CrossRef]
21. Liu, J.; Liu, Y.; Liu, N.; Han, Y.; Zhang, X.; Huang, H.; Lifshitz, Y.; Lee, S.; Zhong, J.; Kang, Z. Metal-free efficient photocatalyst for stable visible water splitting via a two-electron pathway. *Science* **2015**, *347*, 970–974. [CrossRef]

22. Wang, G.; Li, D.; Sun, Q.; Dang, S.; Zhong, M.; Xiao, S.; Liu, G. Hybrid density functional study on the photocatalytic properties of two-dimensional g-ZnO based heterostructures. *Nanomaterials* **2018**, *8*, 374. [CrossRef]
23. Wang, G.; Dang, S.; Zhang, P.; Xiao, S.; Wang, C.; Zhong, M. Hybrid density functional study on the photocatalytic properties of AlN/$MoSe_2$, AlN/WS_2, and AlN/WSe_2 heterostructures. *J. Phys. D Appl. Phys.* **2018**, *51*, 025109. [CrossRef]
24. Wang, G.; Dang, S.; Zhao, W.; Li, Y.; Xiao, S.; Zhong, M. Tunable photocatalytic properties of GaN-based two-dimensional heterostructures. *Phys. Status Solidi B* **2018**. [CrossRef]
25. Liang, D.; Jing, T.; Ma, Y.; Hao, J.; Sun, G.; Deng, M. Photocatalytic properties of g-C_6N_6/g-C_3N_4 heterostructure: a theoretical study. *J. Phys. Chem. C* **2016**, *120*, 24023–24029. [CrossRef]
26. Li, J.; Liu, E.; Ma, Y.; Hu, X.; Wan, J.; Sun, L.; Fan, J. Synthesis of MoS_2/g-C_3N_4 nanosheets as 2D heterojunction photocatalysts with enhanced visible light activity. *Appl. Surf. Sci.* **2016**, *364*, 694–702. [CrossRef]
27. Wang, H.; Li, X.; Yang, J. The g-C_3N_4/C_2N nanocomposite: A g-C_3N_4-based water-splitting photocatalyst with enhanced energy efficiency. *ChemPhysChem* **2016**, *17*, 2100–2104. [CrossRef]
28. Li, J.; Wei, W.; Mu, C.; Huang, B.; Dai, Y. Electronic properties of van der Waals g-C_3N_4/CdS heterojunction from first-principles. *Phys. E* **2018**, *103*, 459–463. [CrossRef]
29. Perdew, J.P.; Burke, K.; Ernzerhof, M. Generalized gradient approximation made simple. *Phys. Rev. Lett.* **1996**, *77*, 3865. [CrossRef]
30. Ernzerhof, M.; Scuseria, G.E. Assessment of the Perdew-Burke-Ernzerhof exchange-correlation functional. *J. Chem. Phys.* **1999**, *110*, 5029–5036. [CrossRef]
31. Heyd, J.; Scuseria, G.E.; Ernzerhof, M. Hybrid functionals based on a screened Coulomb potential. *J. Chem. Phys.* **2003**, *118*, 8207–8215. [CrossRef]
32. Kresse, G.; Furthmüller, J. Efficient iterative schemes for ab initio total-energy calculations using a plane-wave basis set. *Phys. Rev. B* **1996**, *54*, 11169. [CrossRef]
33. Blöchl, P.E. Projector augmented-wave method. *Phys. Rev. B* **1994**, *50*, 17953. [CrossRef]
34. Grimme, S.; Antony, J.; Ehrlich, S.; Krieg, H. A consistent and accurate ab initio parametrization of density functional dispersion Ccorrection (DFT-D) for the 94 elements H-Pu. *J. Chem. Phys.* **2010**, *132*, 154104. [CrossRef]
35. Monkhorst, H.J.; Pack, J.D. Special points for Brillouin-zone integrations. *Phys. Rev. B* **1976**, *13*, 5188–5192. [CrossRef]
36. Saha, S.; Sinha, T.P.; Mookerjee, A. Electronic structure, chemical bonding, and optical properties of paraelectric $BaTiO_3$. *Phys. Rev. B* **2000**, *62*, 8828–8834. [CrossRef]
37. Tian, F.; Liu, C. DFT description on electronic structure and optical absorption properties of anionic S-doped anatase TiO_2. *J. Phys. Chem. B* **2006**, *110*, 17866–17871. [CrossRef]
38. Fu, Q.; Li, J.L.; He, T.; Yang, G.W. Band-engineered $CaTiO_3$ nanowires for visible light photocatalysis. *J. Appl. Phys.* **2013**, *113*, 37. [CrossRef]
39. Bjorkman, T.; Gulans, A.; Krasheninnikov, A.V.; Nieminen, R.M. Van der Waals bonding in layered compounds from advanced density-functional first-principles calculations. *Phys. Rev. Lett.* **2012**, *108*, 235502. [CrossRef]
40. Scalise, E.; Houssa, M.; Pourtois, G.; Ev, V.A.; Stesmans, A. Strain-induced semiconductor to metal transition in the two-dimensional honeycomb structure of MoS_2. *Nano Res.* **2012**, *5*, 43–48. [CrossRef]
41. Yu, W.; Zhu, Z.; Zhang, S.; Cai, X.; Wang, X.; Niu, C.; Zhang, W. Tunable electronic properties of GeSe/phosphorene heterostructure from first-principles study. *Appl. Phys. Lett.* **2016**, *109*, 103104. [CrossRef]
42. Li, S.; Wang, C.; Qiu, H. Single- and few-layer ZrS_2 as efficient photocatalysts for hydrogen production under visible light. *Int. J. Hydrogen Energy* **2015**, *40*, 15503–15509. [CrossRef]
43. Chakrapani, V.; Angus, J.C.; Anderson, A.B.; Wolter, S.D.; Stoner, B.R.; Sumanasekera, G. Charge transfer equilibria between diamond and an aqueous oxygen electrochemical redox couple. *Science* **2007**, *318*, 1424–1430. [CrossRef]
44. Artrith, N.; Sailuam, W.; Limpijumnong, S.; Kolpak, A.M. Reduced overpotentials for electrocatalytic water splitting over Fe- and Ni-modified $BaTiO_3$. *Phys. Chem. Chem. Phys.* **2016**, *18*, 29561–29570. [PubMed]
45. Kishore, M.R.A.; Ravindran, P. Tailoring the electronic band gap and band edge positions in the C_2N Monolayer by P and As substitution for photocatalytic water splitting. *J. Phys. Chem. C* **2017**, *121*, 22216–22224. [CrossRef]

46. Yang, H.; Li, J.; Yu, L.; Huang, B.; Ma, Y.; Ying, D. Theoretical study on electronic properties of in-plane CdS/ZnSe heterostructure: Type-II band alignment for water splitting. *J. Mater. Chem. A* **2018**, *6*, 4161–4166. [CrossRef]
47. Wang, B.; Li, X.; Zhao, R.; Cai, X.; Yu, W.; Li, W.; Liu, Z.; Zhang, L.; Ke, S. Electronic structures and enhanced photocatalytic properties of blue phosphorene/BSe van der Waals heterostructures. *J. Mater. Chem. A* **2018**, *6*, 8923–8929. [CrossRef]